Progress in PHOTOVOLTAICS

PROGRESS IN PHOTOVOLTAICS: RESEARCH AND APPLICATIONS
Prog. Photovolt: Res. Appl. 2015; **23**:1697–1705
Published online in Wiley Online Library (wileyonlinelibrary.com). DOI: 10.1002/pip.2716

ACCELERATED PUBLICATION

Photoluminescence and electroluminescence imaging of perovskite solar cells

Ziv Hameiri[1]*, Arman Mahboubi Soufiani[1], Mattias K. Juhl[1], Liangcong Jiang[2], Fuzhi Huang[2], Yi-Bing Cheng[2], Henner Kampwerth[1], Juergen W. Weber[3], Martin A. Green[1] and Thorsten Trupke[1]

[1] The University of New South Wales, Sydney 2052, NSW, Australia
[2] Monash University, Melbourne 3800, Victoria, Australia
[3] BT Imaging, Sydney 2017, NSW, Australia

ABSTRACT

Fast camera-based luminescence-imaging measurements on perovskite solar cells are presented. The fundamental correlation between the luminescence intensity and the open circuit voltage predicted by the generalised Planck law is confirmed, enabling various quantitative methods for the detection of efficiency-limiting defects to be applied to this new cell structure. Interstinegly, it is found that this fundamental correlation is valid only for light-soaked devices. Copyright © 2015 John Wiley & Sons, Ltd.

KEYWORDS
photoluminescence; electroluminescence; perovskite; imaging

***Correspondence**
Ziv Hameiri, The University of New South Wales, Sydney 2052, NSW, Australia.
E-mail: ziv.hameiri@gmail.com

Received 17 July 2015; Revised 2 October 2015; Accepted 12 October 2015

1. INTRODUCTION

In the last few years, solar cells based on mixed organic–inorganic hybrid perovskites have stunned the photovoltaic community. Although the first efficiency of a solid-state perovskite solar cell of 9.7% was reported only in 2012 [1], rapid progress by several research groups [2–6] has improved this efficiency to an independently confirmed value of 20.1% earlier this year [7]. In less than three years, perovskite solar cells achieved performance levels comparable with those of much more mature thin film solar cell technologies (such as CdTe and CIGS), which took up to ten times as long to reach similar efficiencies [7]. Development of various fabrication methods [4,5,8,9] and several device structures [4,5,10] suggest that this efficiency is still far from its limit.

Despite an astonishing performance improvement in such a short time, perovskite-based solar cells suffer from some major problems. One key challenge for this technology appears to be the stability of the devices [11]; cells tend to undergo degradation (sometimes within only a few hours if not encapsulated properly), especially upon exposure to high temperature and humidity [12,13]. Key electronic material and device properties, such as bulk doping and series resistance, tend to change once exposed to light [14]. Another challenge associated with perovskite-based solar cells, which is common to all thin film solar cell approaches, is the process uniformity. To date, perovskite solar cells have been fabricated mostly on relatively small substrates (generally smaller than $10 \times 10\,mm^2$); however, commercial applications require scaling-up the process to a much larger substrate area (on the order of at least $156 \times 156\,mm^2$). This scaling-up requires the ability to monitor the uniformity of the fabrication process. Lateral process variations can be expected particularly for solution-spreading techniques that are commonly used for the fabrication of perovskite solar cells.

Over the last decade, spatially resolved photoluminescence (PL) and electroluminescence (EL) imaging techniques have been proven to be very powerful monitoring tools for silicon wafers and silicon-based solar cells and modules [15–17]. For silicon devices, PL and EL imaging is frequently used to monitor essential electrical parameters such as minority carrier lifetime [18], implied open circuit voltage [19], diode saturation current [20–22], series

resistance [23], shunt resistance [24] and many more [25]. These methods provide the relevant parameters with high spatial resolution and can be performed with very short measurement time. PL has the added benefit that it is contactless and can therefore be applied to partially processed devices.

Various PL measurement techniques have been applied to perovskite thin films; however, those measurements are limited primarily to spectral and transient PL decay measurements [26–28]. Recently, a method based on the correlation between microscope images and spatially resolved PL decay data was presented [29]. However, this method, similar to all other characterisation methods used to date for perovskite solar cells, is limited to the micron-scale and is not practical for measuring large area device. As a point-by-point raster-scanning (i.e. mapping) technique, it is also inherently slow compared with the camera-based imaging approach, for which the first data on perovskite cells are presented in this study. Only a few milliseconds exposure time were required for all measurements presented later.

The ability to obtain quantitative information from luminescence about various electrical and material parameters is based on the generalised Planck's emission law [30,31]. This study validates the predictions according to the generalised Planck equation for perovskite cells. This fundamental finding enables the use and adaptation of the above wide range of analysis techniques to perovskite-based cells. The paper presents PL and EL images on perovskite-based solar cells and demonstrates their use to identify various efficiency-limiting mechanisms.

2. SOLAR CELLS PREPARATION AND MEASUREMENT SYSTEM

Several $10 \times 10\,mm^2$ planar heterojunction perovskite solar cells were fabricated using a well-documented process [8]. The diagram of this device is shown in Figure 1. Briefly, a dense titanium dioxide (TiO_2) blocking layer was deposited on a clean fluorine-doped tin oxide (FTO) glass by pyrolysis spray of a bis(isopropoxide)–bis(acetylacetonate)–titanium(IV) solution at 450 °C. After cooling down to room temperature, a perovskite film was formed by spin coating of $CH_3NH_3PbI_3$ dimethylformamide (DMF) solution (prepared from PbI_2 and CH_3NH_3 in a molar ratio of 1:1) with the assistance of a gas flow. The substrate was then annealed at 100 °C on a hotplate for 10 min. After cooling down to room temperature, the hole-transporting material (HTM), a Spiro-OMeTAD solution [prepared by dissolving Spiro-OMeTAD in chlorobenzene, together with lithium bis(trifluoromethylsulphonyl)-imide in acetonitrile and 4-tert-butylpyridine] was coated on the perovskite film by spin coating, followed by a thermal deposition of 80 nm of gold. The device was then encapsulated by a cover glass with ultraviolet-curable adhesive [32]. More information regarding the fabrication can be found elsewhere [8]. Figure 1 provides the current–voltage curves of representative solar cells as measured under a standard air mass of 1.5G [33] at 25 °C, together with their key electrical parameters. The measurements were made on a defined area using a mask with a circular aperture (4.5 mm diameter) and a voltage sweep rate of 17 mV/s.

A commercially available one mega-pixel silicon charge-coupled device camera was used to detect the luminescence signal. The illumination was provided by a commercially available 40 W 640 nm light-emitting diode (LED) fitted with a short-pass filter. The illumination intensity was monitored by a calibrated silicon sensor. To prevent detection of LED light reflected from the sample surface, a set of optical filters resulting in a bandpass was placed between the sample and the camera. For EL images, the solar cell was forward biased, while monitoring the applied voltage and the terminal current. Spectral luminescence in the range 700–1000 nm was

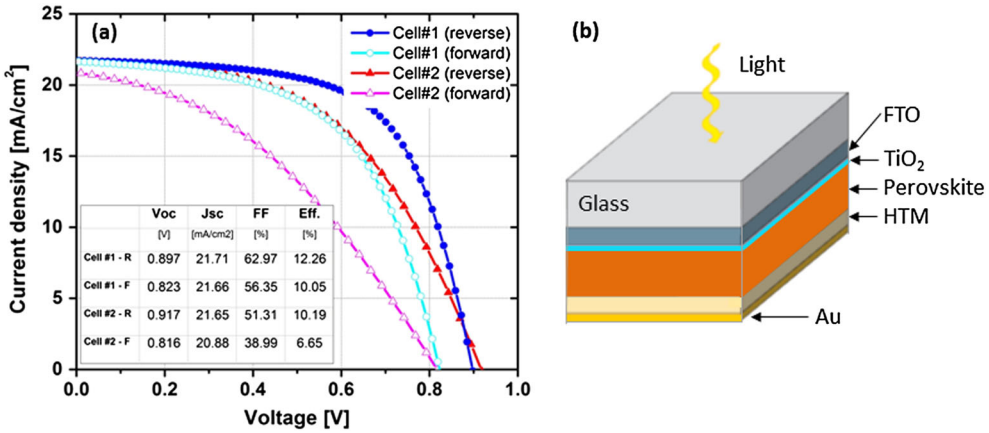

Figure 1. (a) Current density as a function of voltage of representative perovskite solar cells used in this study. The measurements were carried out at voltage sweep rate of 17 mV/s under illumination intensity of 100 mW/cm^2 and a standard air mass of 1.5G [using a class AAA solar simulator (Oriel model 94023A)] at 25 °C. Forward measurements were performed from short circuit to open circuit, while reverse measurements were performed from open circuit to short circuit. (b) Diagram of the solar cell structure was used in this study. FTO, fluorine-doped tin oxide; TiO_2, titanium dioxide; HTM, hole-transporting material; Au, gold.

DOI: 10.1002/pip

measured using an IsoPlane-160 spectrometer (Princeton Instruments).

3. RESULTS AND DISCUSSION

Figure 2 presents luminescence spectra of a representative perovskite solar cell. Both PL and EL spectra are shown; the PL measurement was performed with an incident photon flux of 2.2×10^{16} cm^{-2}.s^{-1}, corresponding to an electrical current density of 3.5 mA/cm^2 (about 0.1 suns), while the EL measurement was carried out using a forward bias voltage of 1.4 V. In order to compare between the two spectra, the EL peak intensity was scaled to match the PL peak intensity. Both emissions have a similar full width at half maximum and a similar location of the peak intensity (783 nm); the peak position is in the range reported by others [34,35]. Significant deviations between the spectra can be observed in the short (<750 nm) and long (>810 nm) wavelength ranges. To clarify this observation, the PL spectra of a test sample containing only an FTO and a TiO_2 layers was measured under the same light intensity. The relatively constant PL emission of this test structure in the wavelength range 735–810 nm and the long tail in the wavelength range above 810 nm explains the deviation between the PL and the EL, since the FTO–TiO_2 structure emits luminescence only under illumination and not under forward bias voltage. As the quantitative analysis methods described in the paper rely on the luminescence from the active absorber of the solar cell, the optical filter set of the measurement system was designed to restrict the detected signal to the spectral range 750 to 850 nm in order to minimise the contribution of the FTO and TiO_2 to the measured PL signal.

Luminescence emission by direct and indirect transitions can be described by the generalised Planck's emission law [30,31]. This generalisation is valid for optical transitions occurring between two bands of energy states that are separated by an energy gap and occupied according to separate thermal distributions, each characterised by separate quasi-Fermi energies [31,36]. It has been derived theoretically and validated experimentally for direct [37] and for indirect [38] semiconductors. According to this emission law, the rate of spontaneous emission $dr_{em}(\hbar\omega)$ of photons with energy between $\hbar\omega$ and $\hbar\omega+d\hbar\omega$ into a solid angle Ω is given by the absorption coefficient $\alpha(\hbar\omega)$ and the difference of the quasi-Fermi energies $\Delta\eta$ as follows [36,39]:

$$dr_{em}(\hbar\omega)=\alpha(\hbar\omega)\frac{c_\gamma D_\gamma \Omega}{\exp\left(\frac{\hbar\omega-\Delta\eta}{kT}\right)-1}d(\hbar\omega) \quad (1)$$

where c_γ is the velocity of the photons in an emitting medium with a refractive index n ($c_\gamma=c_0/n$, where c_0 is the speed of light in vacuum), D_γ is the density of states per solid angle for photons in the medium, k is Boltzmann's constant and T is the temperature in Kelvins. In the case where $(\hbar\omega-\Delta\eta)>>kT$, such as in this study, Boltzmann approximation is valid, and Eq. (1) can be written in a simpler form as follows:

$$dr_{em}(\hbar\omega)=\alpha(\hbar\omega)\exp\left(\frac{-\hbar\omega}{kT}\right)c_\gamma D_\gamma\Omega\,\exp\left(\frac{\Delta\eta}{kT}\right)d(\hbar\omega). \quad (2)$$

The detected luminescence R_{det} can be determined by integrating Eq. (2) [or equally Eq. (1)] and taking into account multiple reflections from both the surfaces and the quantum efficiency of the detection system.

The value of $\Delta\eta$ in the absorber of a solar cell upon illumination represents a fundamental upper limit for the open circuit voltage of the device. For silicon solar cells, the exponential relationship between PL intensity and $\Delta\eta$ has been used to extract quantitative implied voltages from partially processed cells. An exponential relationship of the form

$$R_{det}\propto\exp\left(\frac{qV}{kT}\right)=\exp\left(\frac{V}{v_t}\right) \quad (3)$$

is expected between R_{det} and the device terminal voltage V (where $v_t=kT/q$ is the thermal voltage), for the cases where there is no voltage drop over a series resistance. This relationship was experimentally demonstrated for silicon [38], CIGS [40] and dye sensitised [36] solar cells.

To verify this relationship for perovskite-based solar cells, PL-imaging measurements were performed, and the average PL count (representing the detected PL intensity) from a fully processed cell was recorded together with the measured terminal voltage, while varying the illumination intensity between 0.1 and 0.02 suns. Before the measurement, the solar cell was light soaked for approximately 20 min under 0.1 suns (at room temperature). Figure 3 plots the PL counts in arbitrary units (a.u) on a logarithmic scale together with a best fit to an exponential function [as expected from Eq. (3)]. The obtained good fit (open triangles and dashed line) verifies the exponential relationship between the PL and the terminal voltage.

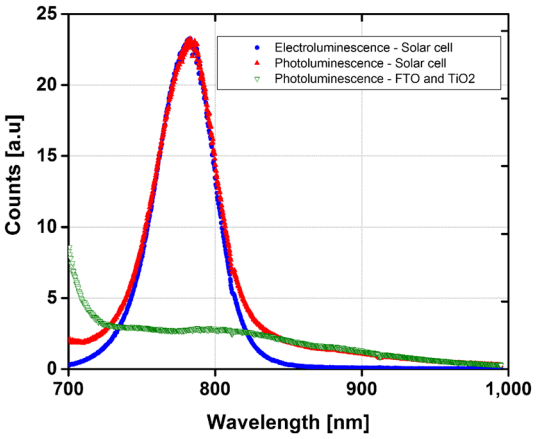

Figure 2. Luminescence spectra of a completed perovskite solar cell and of the FTO-TiO_2 test structure.

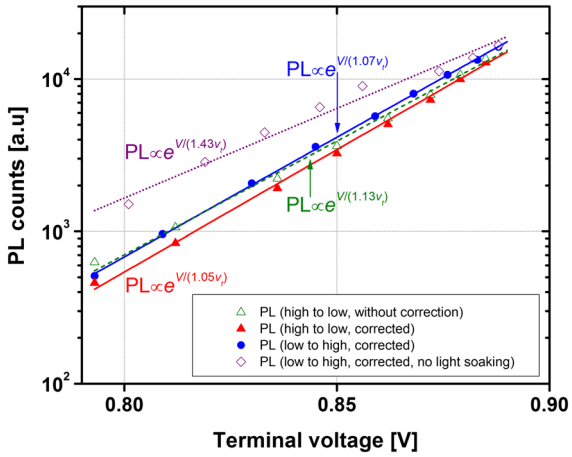

Figure 3. Photoluminescence counts as a function of terminal voltage for measurements: (open triangle) from high to low intensity (including the PL emission from the FTO and TiO_2); (filled triangle) from high intensity to low intensity; (filled circles) from low to high intensity; and (open diamond) from low to high intensity without a light soaking. For corrected values, the PL emission from the FTO and TiO_2 was removed.

However, a larger exponential factor was calculated from the slope ($1.13\times v_t$ instead of the predicted v_t). Spurious PL emission from non-active layers in the device (such as FTO and TiO_2) partly explains these deviations. In order to separate the PL of the active layers from the non-active layers, the PL emission of a FTO–TiO_2 test sample (i.e. an otherwise identical sample but with no active absorber) was measured at the same light intensities. The PL from the active layers was then determined by subtraction of the PL from the non-active layers (FTO–TiO_2) from the PL emitted by the perovskite solar cell. The good fit to an exponential function (filled symbols and solid lines in Figure 3) and the exponential factors in the range $1.05\times v_t$–$1.07\times v_t$ verify the relationship between luminescence and voltage as predicted by Eq. (3). Note that although a small hysteresis was observed when performing the measurement from low to high intensity, a similar exponential factor was detected. This is the first time that this fundamental relationship is demonstrated for perovskite-based solar cells; this finding enables the use of the wide range of EL-based and PL-based analysis techniques to perovskite cells.

The small deviation from the expected unity exponential factor can be related to insufficient light soaking. To highlight the effect of light soaking has on the determined factor, the measurement was repeated; however, this time no light soaking was performed. The FTO–TiO_2 corrected curve for the corresponding measurement is also included in Figure 3 (open diamonds). The relatively poor fit (dotted line) and the large exponential factor indicate that before light soaking the relationship between the luminescence and voltage departs from Eq. (3). This can be explained by changes of the electrical field within the device [41–45]. It can also be related to modification of material properties, such as bulk doping, because of illumination [14] and by light-induced electrical processes, such as previously proposed trap filling [14,46,47]. Note that the measurements were carried out at light intensities below 0.1 suns to minimise temperature variations of the device.

Electroluminescence measurements with an applied forward bias in the dark were also performed on the same cell. The relationship between the average EL intensity and the applied forward bias voltage is shown on a semi-logarithmic scale in the insert of Figure 4. The values substantially deviate from the straight line expected from Eq. (3). In a simplified equivalent circuit, a solar cell is described as a series connection of a diode representing the cell and a resistor, representing the finite series resistance R_s associated with current transport from the terminals to the absorber. The current I associated with a forward bias causes a voltage drop $R_s \times I$ across the series resistance and a corresponding deviation between the terminal voltage and the electrochemical potential difference in the absorber. Such series resistance effects can be compensated by plotting the measured luminescence over the R_s-corrected forward voltage V_{corr} [$V_{corr} = V_{forward} - (R_s \times I)$]. Here, R_s is used as a variable parameter; for this cell, the expected exponential relationship was found for $R_s = 19.2\,\Omega$, which is within the range of R_s values determined from the current–voltage measurements. A similar exponential factor (1.06) as reported before for the PL data was determined. With this simple correction, the exponential dependence is confirmed, and in addition, the ability to extract quantitative series resistance information from luminescence data is demonstrated, an ability which can be exploited further for spatially resolved R_s imaging.

Figure 5 shows PL and EL images of a perovskite solar cell (Cell 1 of Figure 1). Images were taken with a collection time (exposure time) of 0.8 s. Note that although both

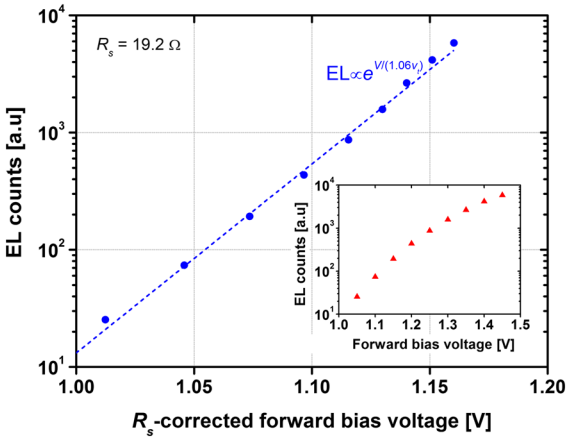

Figure 4. Electroluminescence counts as a function of the series resistance-corrected forward bias voltage [$V_{corr} = V_{forward} - (R_s \times I)$, where I is the measured current and $R_s = 19.2\,\Omega$ for this solar cell].

images are presented with an identical scale (number of counts), they were taken under different excitation conditions (0.1 sun illumination for PL vs forward bias voltage of 1.45 V for EL). We first focus on the PL image [Figure 5 (a)]. Equation (3) correlates high PL counts with high local voltages; Figure 5(a) therefore presents a spatially resolved map of the implied voltage variation across the solar cell, where bright regions indicate regions with higher local voltages (i.e. higher material quality and thus effective carrier lifetime). A significant non-uniformity is detected for this solar cell. This non-uniformity can arise from a number of reasons including the spin coating of the $CH_3NH_3PbI_3$ DMF and the spin coating of the HTM (Spiro-OMeTAD) solutions [5,9]. This image illustrates the significance of macroscopic scale PL imaging to provide spatially resolved images of key electrical parameters

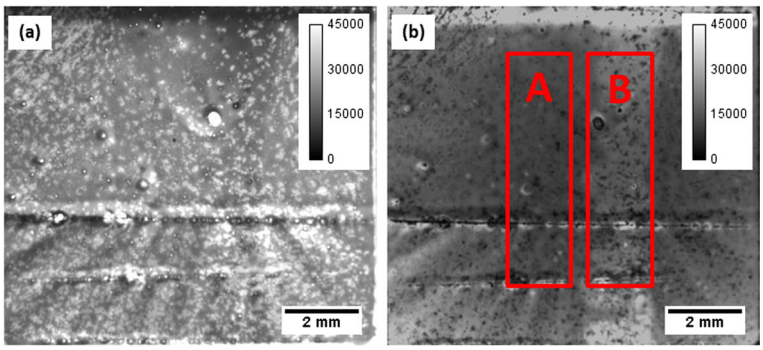

Figure 5. (a) Photoluminescence image (under an illumination of 0.1 suns); and (b) EL image (under a forward bias voltage of 1.45 V) of a perovskite solar cell (Cell 1 of Figure 1). Images were taken with an exposure time of 0.8 s.

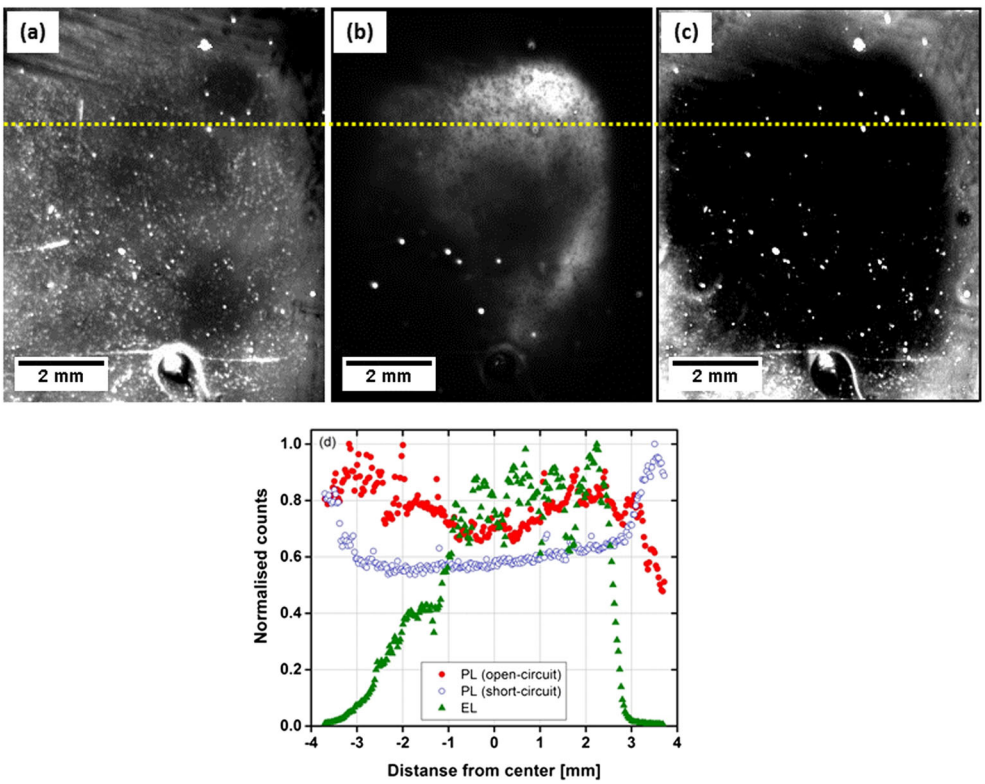

Figure 6. (a) Photoluminescence image (under illumination of 0.1 suns); (b) EL image (under forward bias voltage of 1.45 V); (c) short-circuit PL image (under illumination of 0.1 suns); and (d) a normalised line scans [location is marked with dotted lines in (a)–(c)] of a perovskite solar cell (Cell 2 of Figure 1). Note the opposite behaviour of the EL and the short-circuit PL at the edges.

in a timescale of second or less; no other technique can provide similar information in such a short time. This is an important practical aspect because overcoming non-uniformities is a key capability for a successful scale-up process, which is necessary in any attempts to make perovskite solar cells viable for large scale applications.

The EL image is impacted not only by the local material quality, but also by R_s, as discussed earlier. The contrast between regions A and B in Figure 5(b) cannot be seen in the PL image [Figure 5(a)] and therefore can be associated with R_s. In the darker regions, a larger amount of the external bias voltage is dropped across R_s, and consequently, the EL emission from these areas is reduced. Possible reasons for the observed variation of R_s can be non-uniformity of the FTO, the HTM or the TiO_2 layers. Combination of PL and EL images (or of PL images taken at various operating conditions [23]) can be used to create a spatially resolved map of R_s.

Figure 6 provides an additional example for the use of PL and EL images to identify regions with high R_s. It presents PL and EL images of Cell 2 of Figure 1; the current–voltage measurement indicates that this specific solar cell suffers from a very high R_s (in the range of 75 Ω). Although the PL image [Figure 6(a)] demonstrates a large non-uniformity across the cell, it does not indicate a substantial variation between the edges and the centre [except of the top-right corner; see the line-scan in Figure 6 (d)]. In contrast, the EL image [Figure 6(b)] reveals significant variation with lower intensity near the edges compared with the centre of the device. We assign this variation to high R_s at the edges of the cell. A PL image that was taken under short-circuit condition [Figure 6(c)] supports this conclusion; it presents an opposite contrast to that of the EL image [compare the two representative line scans in Figure 6(d)]. Under short-circuit condition, regions that are directly connected to the terminal will be forced to a zero potential; hence, regions will not emit PL, while areas that are insulated from the terminal by R_s will be under a non-zero potential and therefore PL will be emitted from these locations. These observations are in perfect analogy to equivalent measurements on crystalline silicon solar cells.

Figure 7 demonstrates the application of PL or EL images to monitor the quality of a process (either a fabrication or a measurement process). It presents EL images of a solar cell before [Figure 7(a)] and after [Figures 7(b) and 7(d)] current–voltage measurement using a set of three sequential measurements at low voltage sweep rate (13.4 mV/s). The darker circle in Figure 7(b) corresponds to the location of the aperture that was placed over the cell during these measurements. Since the darker feature can be also seen in the PL image [Figure 7(c)], it can be assigned to reduced localised voltage as a result of local material degradation during the measurement. It was noticed that this reduction is a result of a cumulative effect and is significantly impacted by the number of measurements, the interval between them and the sweep rate. This degradation was clearly noticed by a measured drop of 10 mV of the open circuit voltage. In this case, the luminescence images directly correlate the degradation with the previous measurement and not with an inherent degradation of the material overtime. Spectral PL measurements on this sample within and outside the perturbed region did not detect a shift of the peak intensity or any change of the full width at half maximum. Possible explanation for this effect can be the migration of ions to the surface [48–50]. Note that this degradation was found to be changeable; the degraded region recovers after a few hours [Figure 7(d)].

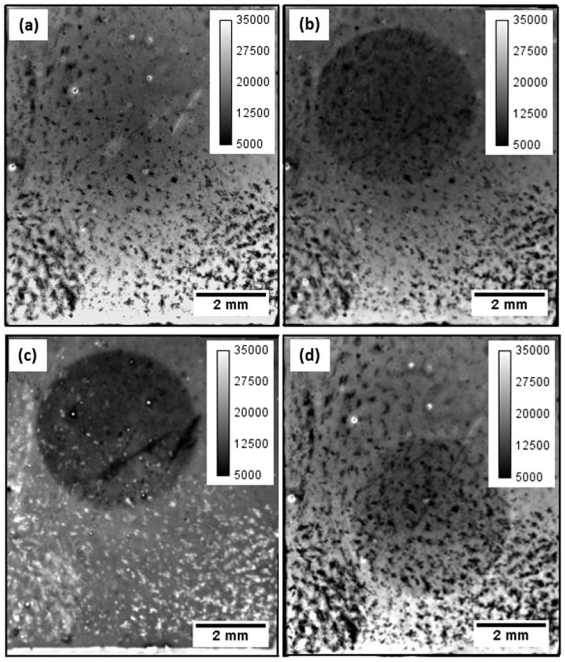

Figure 7. Luminescence images of a perovskite solar cell before (a) and after (b–d) a sequence of three current–voltage measurements using a slow voltage sweep rate (13.4 mV/s): (a) EL image before this sequence; (b) EL image after this sequence; (c) PL image after this sequence; and (d) EL image of the same solar cell after 24 hours of storage and after this measurement sequence was carried out at different location. The EL images were taken under a forward bias voltage of 1.45 V; the PL image was taken at open circuit condition.

4. CONCLUSIONS

The exponential dependence of the luminescence emission on the electrochemical potential difference in the absorber, as predicted by Planck's emission law, was confirmed for perovskite-based solar cells. The expected exponential dependence was demonstrated for PL and also for EL after a correction was made to account for the voltage drop across the series resistance. This fundamental finding enables the use of PL and EL imaging for a wide range of analysis techniques to perovskite-based cells. The ability to extract the series resistance was demonstrated here as an example.

It was noticed that before light soaking, the exponential dependence has a factor larger than predicted by Planck's emission equation. It is assumed that electrical field within the sample alter the carrier distribution and thus the luminescence emission upon illumination.

Quick and powerful luminescence-based imaging techniques were facilitated investigations of the impact of various device-processing conditions on the electronic properties of perovskite solar cells; the usefulness of macroscopic scale PL and EL images to detect non-uniformity across the solar cell was demonstrated. Examples were given for the cases where this non-uniformity can be associated with variation of the localised voltage and for cases where a variation of the series resistance is the dominated mechanism. Luminescence-imaging data will be a rich resource for further development and optimisation of this promising new solar cell type.

ACKNOWLEDGEMENTS

The authors thank Murad Tayebjee and Michael Pollard (both from UNSW) for assistance with the spectral PL measurements and Anita Ho-Baillie (UNSW) for a fruitful collaboration. The authors acknowledge support from the Australian Government through the Australian Renewable Energy Agency (ARENA, Projects 2014/RND097 and 1-GER010) and the Australian Centre for Advanced Photovoltaics (ACAP). The views expressed herein are not necessarily the views of the Australian Government, and the Australian Government does not accept responsibility for any information or advice contained herein. Z. H. acknowledges the support of the Australian Research Council (ARC) through the Discovery Early Career Researcher Award (DECRA, Project DE150100268).

REFERENCES

1. Kim H-S, Lee C-R, Im J-H, Lee K-B, Moehl T, Marchioro A, Moon S-J, Humphry-Baker R, Yum J-H, Moser J, Gratzel M, Park N-G. Lead iodide perovskite-sensitized all-solid-state submicron thin film mesoscopic solar cell with efficiency exceeding 9%. *Scientific Reports* 2012; **2**: 591.
2. McGehee MD. Perovskite solar cells: Continuing to soar. *Nature materials* 2014; **13**: 845–846.
3. Green M, Ho-Baillie A, Snaith H. The emergence of perovskite solar cells. *Nature Photonics* 2014; **8**: 506–514.
4. Burschka J, Pellet N, Moon S-J, Humphry-Baker R, Gao P, Nazeeruddin MK, Gratzel M. Sequential deposition as a route to high-performance perovskite-sensitized solar cells. *Nature* 2013; **499**: 316–319.
5. Liu M, Johnston MB, Snaith HJ. Efficient planar heterojunction perovskite solar cells by vapour deposition. *Nature* 2013; **501**: 395–398.
6. Jeon NJ, Noh JH, Yang WS, Kim YC, Ryu S, Seo J, Seok SI. Compositional engineering of perovskite materials for high-performance solar cells. *Nature* 2015; **517**: 476–480.
7. Best research cell efficiencies (version 27/4/2015—http://www.nrel.gov/ncpv/), National Center for Photovoltaics, National Renewable Energy Laboratory (USA), last accessed: 10/07/2015.
8. Huang F, Dkhissi Y, Huang W, Xiao M, Benesperi I, Rubanov S, Zhu Y, Lin X, Jiang L, Zhou Y, Gray-Weale A, Etheridge J, McNeill C, Caruso R, Bach U, Spiccia L, Cheng Y-B. Gas-assisted preparation of lead iodide perovskite films consisting of a monolayer of single crystalline grains for high efficiency planar solar cells. *Nano Energy* 2014; **10**: 10–18.
9. Chen Q, Zhou H, Hong Z, Luo S, Duan H-S, Wang H-H, Liu Y, Li G, Yang Y. Planar heterojunction perovskite solar cells via vapor-assisted solution process. *Journal of the American Chemical Society* 2014; **136**: 622–625.
10. Heo JH, Im SH, Noh JH, Mandal TN, Lim C-S, Chang JA, Lee YH, Kim H-J, Sarkar A, NazeeruddinMd K, Gratzel M, Seok SI. Efficient inorganic–organic hybrid heterojunction solar cells containing perovskite compound and polymeric hole conductors. *Nature Photonics* 2013; **7**: 486–491.
11. Green MA, Bein T. Photovoltaics: Perovskite cells charge forward. *Nature Materials* 2015; **14**: 559–561.
12. Gratzel M. The light and shade of perovskite solar cells. *Nature Materials* 2014; **13**: 838–842.
13. Han Y, Meyer S, Dkhissi Y, Weber K, Pringle JM, Bach U, Spiccia L, Cheng Y-B. Degradation observations of encapsulated planar $CH_3NH_3PbI_3$ perovskite solar cells at high temperatures and humidity. *Journal of Materials Chemistry A* 2015; **3**: 8139–8147.
14. Stranks SD, Burlakov VM, Leijtens T, Ball JM, Goriely A, Snaith HJ. Recombination kinetics in organic–inorganic perovskites: Excitons, free charge, and subgap states. *Physical Review Applied* 2014; **2**: 034007.
15. Trupke T, Bardos RA, Schubert MC, Warta W. Photoluminescence imaging of silicon wafers. *Applied Physics Letters* 2006; **89**: 044107.
16. Abbott MD, Cotter JE, Chen FW, Trupke T, Bardos RA, Fisher KC. Application of photoluminescence characterization to the development and manufacturing of high-efficiency silicon solar cells. *Journal of Applied Physics* 2006; **100**: 114514.
17. Trupke T, Mitchell B, Weber JW, McMillan W, Bardos RA, Kroeze R. Photoluminescence imaging

for photovoltaic applications. *Energy Procedia* 2012; **15**: 135–146.
18. Giesecke JA, Schubert MC, Michl B, Schindler F, Warta W. Minority carrier lifetime imaging of silicon wafers calibrated by quasi-steady-state photoluminescence. *Solar Energy Materials and Solar Cells* 2011; **95**: 1011–1018.
19. Shen C, Kampwerth H, Green M. Photoluminescence-based open circuit voltage and effective lifetime images re-interpretation for solar cells: The influence of horizontal balancing currents. *Solar Energy Materials and Solar Cells* 2014; **130**: 393–396.
20. Shen C, Kampwerth H, Green M, Trupke T, Carstensen J, Schütt A. Spatially resolved photoluminescence imaging of essential silicon solar cell parameters and comparison with CELLO measurements. *Solar Energy Materials and Solar Cells* 2013; **109**: 77–81.
21. Müller J, Bothe K, Herlufsen S, Ohrdes T, Brendel R. Reverse saturation current density imaging of highly doped regions in silicon employing photoluminescence measurements. *IEEE Journal of Photovoltaics* 2012; **2**: 473–478.
22. Hameiri Z, Chaturvedi P. Spatially resolved electrical parameters of silicon wafers and solar cells by contactless photoluminescence imaging. *Applied Physics Letters* 2013; **102**: 073502.
23. Kampwerth H, Trupke T, Weber JW, Augarten Y. Advanced luminescence based effective series resistance imaging of silicon solar cells. *Applied Physics Letters* 2008; **93**: 202102.
24. Augarten Y, Trupke T, Lenio M. Calculation of quantitative shunt values using photoluminescence imaging. *Progress in Photovoltaics: Research and Applications* 2013; **21**: 933–941.
25. Michl B, Padilla M, Geisemeyer I, Haag ST, Schindler F, Schubert MC, Warta W. Imaging techniques for quantitative silicon material and solar cell analysis. *IEEE Journal of Photovoltaics* 2014; **4**: 1502–1510.
26. Noel N, Abate A, Stranks S, Parrott E, Burlakov V, Goriely A, Snaith H. Enhanced photoluminescence and solar cell performance via Lewis base passivation of organic–inorganic lead halide perovskites. *ACS Nano* 2014; **8**: 9815–9821.
27. Wen X, Sheng R, Ho-Baillie A, Benda A, Woo S, Ma Q, Huang S, Green M. Green M. Morphology and carrier extraction study of organic–inorganic metal halide perovskite by one- and two-photon fluorescence microscopy. *Journal of Physical Chemistry Letters* 2014; **5**: 3849–3853.
28. Stranks SD, Eperon GE, Grancini G, Menelaou C, Alcocer MJP, Leijtens T, Herz LM, Petrozza A, Snaith HJ. Electron-hole diffusion lengths exceeding 1 micrometer in an organometal trihalide perovskite absorber. *Science* 2013; **342**: 341–344.
29. deQuilettes DW, Vorpahl SM, Stranks SD, Nagaoka H, Eperon GE, Ziffer ME, Snaith HJ, Ginger DS. Impact of microstructure on local carrier lifetime in perovskite solar cells. *Science* 2015; **348**: 683–686.
30. Würfel P. The chemical potential of radiation. *Journal of Physics C: Solid State Physics* 1982; **15**: 3967.
31. Würfel P, Finkbeiner S, Daub E. Generalized Planck's radiation law for luminescence via indirect transitions. *Applied Physics A* 1995; **60**: 67–70.
32. Han Y, Meyer S, Dkhissi Y, Weber K, Pringle JM, Bach U, Spiccia L, Cheng Y-B. Degradation observations of encapsulated planar $CH_3NH_3PbI_3$ perovskite solar cells at high temperatures and humidity. *Journal of Materials Chemistry A* 2015; **3**: 8139–8147.
33. IEC 60904–3: Photovoltaic devices—Part 3: Measurement principles for terrestrial photovoltaic (PV) solar devices with reference spectral irradiance data, 2008.
34. Tress W, Marinova N, Inganäs O, Nazeeruddin M, Zakeeruddin SM, Graetzel M. Predicting the open-circuit voltage of $CH_3NH_3PbI_3$ perovskite solar cells using electroluminescence and photovoltaic quantum efficiency spectra: the role of radiative and non-radiative recombination. *Advanced Energy Materials* 2014; **3**: 1400812.
35. Xing G, Mathews N, Lim SS, Yantara N, Liu X, Sabba D, Grätzel M, Mhaisalkar S, Sum TC. Low-temperature solution-processed wavelength-tunable perovskites for lasing. *Nature Materials* 2014; **13**: 476–480.
36. Trupke T, Würfel P, Uhlendorf I, Lauermann I. Electroluminescence of the dye-sensitized solar cell. *Journal of Physical Chemistry B* 1999; **103**: 1905–1910.
37. Feuerbacher B, Würfel P. Verification of a generalised Planck law by investigation of the emission from GaAs luminescent diodes. *Journal of Physics: Condensed Matter* 1990; **2**: 3803.
38. Schick K, Daub E, Finkbeiner S, Würfel P. Verification of a generalized Planck law for luminescence radiation from silicon solar cells. *Applied Physics A* 1992; **54**: 109–114.
39. Daub E, Würfel P. Ultralow values of the absorption coefficient of Si obtained from luminescence. *Physical Review Letters* 1995; **74**: 1020–1023.
40. Bauer GH, Brüggemann R, Tardon S, Vignoli S, Kniese R. Quasi-Fermi level splitting and identification of recombination losses from room temperature luminescence in $Cu(In_{1-x}Ga_x)Se_2$ thin films versus optical band gap. *Thin Solid Films* 2005; **480–481**: 410–414.
41. Green MA. Do built-in fields improve solar cell performance? *Progress in Photovoltaics: Research and Applications* 2009; **17**: 57–66.

42. Guerrero A, Juarez-Perez EJ, Bisquert J, Mora-Sero I, Garcia-Belmonte G. Electrical field profile and doping in planar lead halide perovskite solar cells. *Applied Physics Letters* 2014; **105**: 133902.
43. Li X, Wang X, Zhang W, Wu Y, Gao F, Fang J. The effect of external electric field on the performance of perovskite solar cells. *Organic Electronics* 2015; **18**: 107–112.
44. Tress W, Marinova N, Moehl T, Zakeeruddin SM, Nazeeruddin MK, Gratzel M. Understanding the rate-dependent *J-V* hysteresis, slow time component, and aging in $CH_3NH_3PbI_3$ perovskite solar cells: The role of a compensated electric field. *Energy and Environmental Science* 2015; **8**: 995–1004.
45. Zhang C, Sun D, Sheng CX, Zhai YX, Mielczarek K, Zakhidov A, Vardeny ZV. Magnetic field effects in hybrid perovskite devices. *Nature Physics* 2015; **11**: 427–434.
46. Wu XX, Trinh MT, Niesner D, Zhu HM, Norman Z, Owen JS, Yaffe O, Kudisch BJ, Zhu XY. Trap states in lead iodide perovskites. *Journal of the American Chemical Society* 2015; **137**: 2089–2096.
47. Wetzelaer G-J, Scheepers M, Sempere A, Momblona C, Ávila J, Bolink H. Trap-assisted non-radiative recombination in organic–inorganic perovskite solar cells. *Advanced Materials* 2015; **27**: 1837–1841.
48. Gottesman R, Haltzi E, Gouda L, Tirosh S, Bouhadana Y, Zaban A, Mosconi E, De Angelis F. Extremely slow photoconductivity response of $CH_3NH_3PbI_3$ perovskites suggesting structural changes under working conditions. *The Journal of Physical Chemistry Letters* 2014; **5**: 2662–2669.
49. Eames C, Frost JM, Barnes PRF, O'Regan BC, Walsh A, Islam MS. Ionic transport in hybrid lead iodide perovskite solar cells. *Nature Communications* 2015; **6**: 7497.
50. Leguy AMA, Frost JM, McMahon AP, Sakai VG, Kockelmann W, Law C, Li X, Foglia F, Walsh A, O'Regan BC, Nelson J, Cabral JT, Barnes PRF. The dynamics of methylammonium ions in hybrid organic–inorganic perovskite solar cells. *Nature Communications* 2015; **6**: 7124.